Nanoscale

Nanoscale

www.rsc.org/nanoscale

ROYAL SOCIETY OF CHEMISTRY

ROYAL SOCIETY OF CHEMISTRY

www.rsc.org/nanoscale

Journal Name

ARTICLE

Constructing bulk defective perovskite SrTiO₃ nanocubes for high performance photocatalyst

Guoqiang Zhang,[a] Wenshuai Jiang,[b] Shixin Hua,[b] Haifeng Zhao,[a] Ligong Zhang[a] and Zaicheng Sun[b*]

Defects (Ti³⁺ or oxygen vacancies) have been demonstrated to promote the charge separation process in TiO₂ based photocatalysts. Especially, the bulk defects within a certain concentration can give a great enhancement for both light absorption and charge separation efficiency. In this report, we explored a one-step molten salts route to synthesize the SrTiO₃ nanocubes with bulk defects (Ti³⁺ doped) by using SrCO₃ as Sr source, TiO₂ and Ti powder as Ti source. The amount of defects can be tuned by changing the molar ratio of Ti/TiO₂. The corresponding bandgap of SrTiO₃ can be changed from 3.29 to 2.73 eV with the increase of defects. X-ray diffraction and electron microscopy disclose that SrTiO₃ has highly crystalline and cubic morphology. X-ray photoelectron spectroscopy and electron paramagnetic resonance indicate that as-prepared SrTiO₃ is close to the Ti³⁺ doped SrTiO₃. Surface photovoltage spectroscopy (SPS) and field-induced SPS confirm that Ti³⁺ dopping results in the SrTiO₃ turns from n-type semiconductor to p-type. The SrTiO₃ with optimal amount defects exhibits highly enhanced photocatalytic performance. Excess amount of defects results in a weak SPS response and photocatalytic performance.

Introduction

Perovskite-type materials have been extensively studied because of their wide applications as catalytic, oxygen-transport, ferroelectric, piezoelectric, and dielectric materials.[1-4] Strontium titanate (SrTiO₃) is a typical perovskite oxide that is capable of tunable chemical and physical properties by altering its composition. For example, it is easily converted into an n-type semiconductor at room temperature by either reduction or doping.[5-10] For that reason, SrTiO₃ has been also investigated as a photocatalytic[11-13] and thermoelectric materials[14, 15]. The pristine SrTiO₃ with a wide bandgap of 3.3 eV exhibits super photo, thermal and chemical stability. Numerous studies have been performed to improve the photocatalytic activity of SrTiO₃, such as tailoring the morphology to increase the surface area,[16-18] doping with heteroatom to tune the bandgap,[6-8, 10] loading the cocatalyst to promote the charge separation.[19, 20] In the photocatalysis processes, the rapid recombination of photo-generated carriers limits the photocatalytic efficiency of SrTiO₃. Recently, it has been demonstrated introducing defects (such as oxygen vacancies) to the photocatalyst, for example TiO₂, can narrow the bandgap and extend the visible light absorption. More importantly, it can greatly promote the charge separation efficiency and enhance the photocatalytic performance of photocatalyst. Our group illustrated that both surface and bulk

defects have a similar function,[21] even the bulk defects work better for visible light photocatalytic activity enhancement.[21-23] Therefore, SrTiO₃ materials with a defective crystal structure and tuned bandgap are interesting and potentially beneficial to photocatalytic applications. The pristine SrTiO₃ could be treated by chemical reduction and arc-melting to obtain SrTiO₃ with surface oxygen vacancies defects.[9, 24] In general, perovskite SrTiO₃ will be produced with small surface area and defect free because it is synthesized via high temperature solid phase synthesis route under air ambient. Although a few groups reported the SrTiO₃ could be synthesized via hydrothermal route, oxygen vacancy free SrTiO₃ was still obtained even in the hydrazine media.[25] It is still a challenge to directly obtain defective SrTiO₃ via chemical synthesis route and keep SrTiO₃ in nanoscale size as well.

Herein, we have developed a simple one-step molten salts route to synthesize SrTiO₃ nanocubes by employing TiO₂ as Ti source, SrCO₃ as Sr source in the NaCl and KCl mixed molten salts at 700 °C. To obtain the defective SrTiO₃, Ti powder was chosen as a secondary Ti source, Ti was partially oxidized in the reaction to form Ti³⁺ doped SrTiO₃, which introduce an impurity energy band below the conduction band of SrTiO₃. That narrows the bandgap of SrTiO₃ from 3.29 to 2.73 eV. The color of SrTiO₃ turns from light blue to dark blue with the increase of oxygen vacancies (Ti³⁺). When the molar ratio of Ti/TiO₂ is about 5:7, the defective SrTiO₃ shows an optimum H₂ production rate of 311.8 μmol/h and 8.48 μmol/h for 50 mg of samples under UV-Vis light and visible light (λ > 420 nm) irradiation, which exhibits 2.7 times (UV-Vis) and 40.4 times (λ > 420 nm) than pristine SrTiO₃. To understand the function of the defects, surface photovoltage spectroscopy was employed to explore the effect of defects on charge separation process. Surface photovoltage

a. State Key Laboratory of Luminescence and Applications, Changchun Institute of Optics, Fine Mechanics and Physics, Changchun, 130033, Jilin, P. R. China.
b. Beijing Key Laboratory of Green Catalysis and Separation Department of Chemistry, Chemical Engineering School of Environmental and Energy, University of Beijing Technology, Beijing, 100022, P. R. China. Email:sunzc@bjut.edu.cn

spectroscopy (SPS) illustrate that the pristine $SrTiO_3$ nanocube exhibits a typical n-type semiconductor character. Introducing Ti^{3+} into $SrTiO_3$ results in a p-type semiconductor nature. Field-induced SPS further confirm the change of conduction type. Excess amount of Ti^{3+} in $SrTiO_3$ may produce a deep energy band as a recombination center for photogenerated charges. Ti^{3+} doping also may alert the conductivity of $SrTiO_3$, these factors result in a weak or disappeared SPS response.

Experimental

Chemicals and Materials

$SrCO_3$ (AR, 99.8%) and Titanium (metal) crushed sponge (Ti, AR, 99.5%) are purchased from Aladdin Reagent Company. Methanol (AR, 99.5%), NaCl (AR, 99.8%) and KCl (AR, 99.8%) are purchased from Sinopharm Chemical Reagent Company. P25 TiO_2 is purchased from Degussa AG, Germany. All chemicals are used without any further purification.

Synthesis of $SrTiO_3$ (0-9:12-3) nanocubes

In the typical synthesis of $SrTiO_3$ nanocubes, $SrCO_3$, Ti powder, TiO_2, NaCl and KCl are mixed in an overall stoichiometric ratio of $1:(x/12):(1 - x/12):50:50$ (x = 0, 3, 4, 5, 6, 7 and 9; Ti/TiO_2 = $x/(12 - x)$). The mixtures are put into an alumina crucible and then heated to 700 °C at a rate of 5 °C/min in a muffle furnace and maintained at this temperature for 5 h. After cooling down to room temperature, the samples are washed with deionized distilled water several times to remove remaining salt impurity and dried in an oven at 60 ℃ for 12 h.

Characterizations

Scanning electron microscope (SEM) images are measured on JEOL JSM 4800F. Transmission electron microscope (TEM) images are taken using an FEI Tecnai G2 operated at 200 kV. The crystalline structure is recorded by using an X-ray diffractometer (XRD) (Bruker AXS D8 Focus), using Cu Kα radiation (λ = 1.54056 Å). Brunauer-Emmett-Teller (BET) specific surface area is measured using a Micromeritics Gemini V Surface Area and Pore Size Analyzer. X-ray photoelectron spectrum (XPS) analyses are performed on an ESCALABMKII spectrometer with an Al-Kα (1486.6 eV) achromatic X-ray source. The UV-Vis absorption spectra are recorded on a UV-3600 UV-Vis-NIR scanning spectrophotometer (Shimadzu). The electron paramagnetic resonance (EPR) spectroscopy was recorded on a JEOL JES-FA200 EPR spectrometer at 9.45 GHz at 300K.

Photocatalytic Activity Measurements

The 50 mg of samples photocatalyst loaded with 1.0 wt% Pt is placed into an aqueous methanol solution (120 mL, 25 voL%) in a closed gas circulation system (Perfect Light Company Labsolar-III (AG)). The UV-Vis light and visible light irradiation are obtained from a 300 W Xe lamp (PLS-SXE 300, Beijing Trusttech Co. Ltd, China) without and with a UVCUT-420 nm filter (Newport), respectively. The evolved gases are detected in situ by using an online gas chromatograph (GC-2014C, Shimadzu) equipped with a thermal conductivity detector (TCD).

Surface Photovoltage Measurements

Surface photovoltage (SPV) measurement system consists of a source of monochromatic light, a lock-in amplifier (SR 830-DSP) with a light chopper (SR 540) and a sample chamber. Monochromatic light is provided by a 300 W Xe lamp (PLS-SXE 300, Beijing Trusttech Co. Ltd, China) and a monochromator (SBP500, Zolix). All measurements are operated at room temperature and under ambient pressure and samples are not pretreated prior to the SPV measurement.

Photoelectrode Preparation

The 50 mg of samples is dispersed in a 100 mL of 0.2 mg/mL I_2/acetone solution under ultrasonic treatment. A two electrode process is used to deposit the samples at the applied potential of 30 V for 5 min. FTO glass substrates with the coated area about 1×3 cm^2 is used for both electrodes. Then, the deposited electrode is dried at 200 °C for 30 min to remove I_2 residues.

Photoelectrochemical Measurements

A conventional three electrode process is used to investigate the photoelectrochemical properties of samples in a quartz cell. A FTO photoanode deposited samples, Ag/AgCl, and Pt foil electrode act as the working electrode, reference electrode, and counter electrode, respectively. A 1.0 M NaOH aqueous solution is used as the electrolyte. The photoanode is illuminated by a 300 W Xe lamp (PLS-SXE 300, Beijing Trusttech Co. Ltd, China) with a monochromator. The illuminated area is

$$IPCE\ (\%) = \frac{1240\ \times photocurrent\ density\ (mA\ cm^{-2})}{wavelength\ (nm)\ \times photon\ flux\ (mW\ cm^{-2})} \times 100$$

about 1×0.5 cm^2. The IPCE (incident photon-to-current conversion efficiency) is calculated as the following equation:

Results and discussion

In general, perovskite oxides were synthesized *via* high temperature solid phase reaction route, leading to a relatively small surface area and low catalytic activity. In addition, the reaction was carried out in the air ambient and high temperature (~ 1200 °C), resulting in an oxygen vacancy free oxide. In order to obtain $SrTiO_3$ with nanostructures, we developed a molten salts route to synthesize $SrTiO_3$ nanocubes using $SrCO_3$ as Sr source and TiO_2 as Ti source. To introduce oxygen vacancies into the $SrTiO_3$ nanocubes, Ti powder was employed as a secondary Ti source. In the reaction, Ti was oxidized to form Ti^{3+} or oxygen vacancies in the $SrTiO_3$ nanotubes. Fig. S1 shows the optical images of $SrTiO_3$ prepared from different molar ratio of Ti/TiO_2 (m/n, where, m = 0-9, n = 12-3, $m + n$ = 12, denoted as $SrTiO_3$ m:n). The color of as-prepared $SrTiO_3$ samples gradually turns from white to light blue and finally into dark blue with increasing the fraction of Ti powder. The blue color indicates that the as-prepared samples may contain Ti^{3+}, in other words, the as-prepared sample contains oxygen vacancies. Fig. S2 and 1A show the scanning

electron microscopy (SEM) images of SrTiO$_3$ *m:n* with cubic morphology and uniformly size. Fig. 1B, S3 and S4 show the transmission electron microscopy (TEM) images, corresponding particles size distribution and high resolution TEM images. TEM images disclose that the side length of nanocubes is about 70 nm. Each nanocubes are a single crystalline particle with clear lattice fringe spacing of 0.276 nm in the (110) direction of SrTiO$_3$. Powder X-ray diffraction (XRD) patterns of SrTiO$_3$ *m:n* are shown in the Fig. S5. All samples exhibit a typical cubic phase with the diffraction peaks at 22.78, 32.42, 39.98, 46.49, 57.80, 67.81 and 77.18 degree, which are related to the (100), (110), (111), (200), (211), (220), (310) of cubic phase SrTiO$_3$ (JCPDS no. 35-0734), and no additional diffraction peaks of other species are observed. According to the Scherrer equation, the nanocubes size is calculated to be ~ 66 nm by using (110) reflection peak, agreeing with the TEM results. Diffused reflective UV-Vis spectroscopy is presented in the Fig. 1C. Compared with SrTiO$_3$ 0:12, a stronger broad absorption band in the visible-light region is observed with the increasing of molar ratio of Ti/TiO$_2$. These results match well with the color change of this series samples (Fig. S1). The Tauc plot of these SrTiO$_3$ is shown in Fig. 1D. The optical bandgap of SrTiO$_3$ changes from 3.29 eV for SrTiO$_3$ 0:12 to 3.16 eV for SrTiO$_3$ 5:7 and finally reaches 2.73 eV for SrTiO$_3$ 9:3. That indicates the bandgap can be tuned by introducing the defects into SrTiO$_3$. According to previous reports,[9, 21, 26] a defect energy band is introduced below the conduction band of SrTiO$_3$, thus narrowed bandgap is observed.
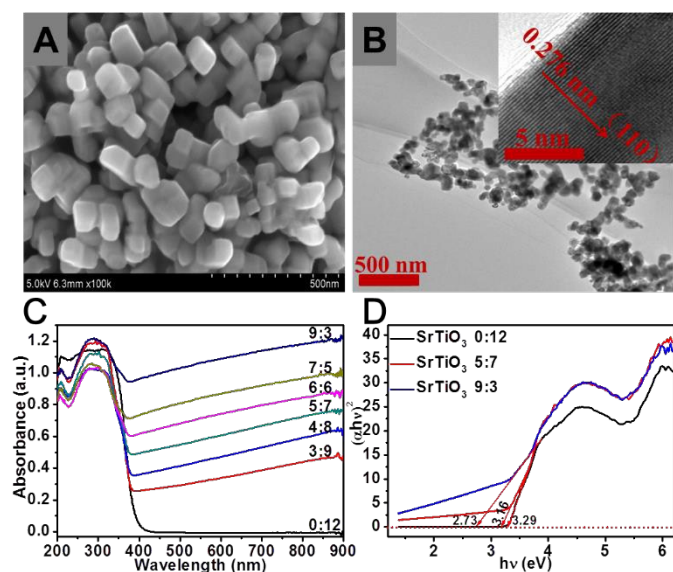
Fig. 1 Field emission scanning electron microscopy (FE-SEM) image (A), transmission electron microscopy (TEM) image (B) and high resolution TEM image (Inset of B) of SrTiO$_3$ 5:7. Diffusion reflection UV-Vis spectra (C) of SrTiO$_3$ (0:12, 3:9, 4:8, 5:7, 6:6, 7:5 and 9:3). D is the Tauc plot of transformed Kubelka-Munk function vs the energy of SrTiO$_3$ (0:12, 5:7 and 9:3).

X-ray photoelectron spectroscopy (XPS, Fig. S6) and electron paramagnetic resonance (EPR) spectra are employed to further confirm as-prepared SrTiO$_3$ with Ti^{3+} or oxygen vacancies. Fig. 2A and 2B show high resolution XPS spectrum of Sr 3d and Ti 2p of SrTiO$_3$ (0:12, 3:9, 5:7 and 9:3). Both the peaks of Sr3d and Ti2p slightly shift to high binding energy gradually with the increasing of molar ratio of Ti/TiO$_2$. This whole XPS peaks shift is a characteristic shift of Fermi level.[27, 28] The defects like

oxygen vacancies and/or Ti^{3+} increase the equilibrium electron density and push the Fermi level upwards and therefore increase the measured binding energies. [9, 29] The O 1s high resolution XPS spectra (Fig. 2C) of SrTiO$_3$ (0:12 and 5:7) can be described as the superposition of three peaks by Gaussian distribution, located around 529.2 eV, 530.0 eV and 531.9 eV, respectively. The O 1s peak at 529.2.eV is usually assigned to bridging oxygen on SrTiO$_3$ surface.[30] The peak at 530.0 eV is associated with the O^{2-} ions in the crystal structure.[9, 31] And the peak at 531.9 eV, is attributed to O^{2-} in the oxygen defects.[9, 32] In the Fig. 2C, the peak at 531.9 eV presents an obvious improvement implying that oxygen vacancy concentration increases compared with SrTiO$_3$ 0:12. As shown in Fig. 2D, the EPR signal observed in SrTiO$_3$ 0:12, 5:7 and 9:3 with g = 1.97 can be attributed to paramagnetic Ti^{3+},[26, 33] and g = 2.00 is assigned to Ti^{3+} in the vicinity of oxygen vacancies in SrTiO$_3$ lattice structure.[34-36] The signal intensity increases from SrTiO$_3$ 0:12 to 9:3, indicating that the oxygen vacancy concentration increases with the increasing of molar ratio Ti/TiO$_2$. The valance band (VB) XPS of SrTiO$_3$ (0:12, 3:9, 5:7 and 9:3) are shown in Fig. S7. The VB of SrTiO$_3$ locates at ~ 1.71 eV below the Fermi level and no obvious shift is observed with the introduction of defects, which keeps same as previous reports[9].
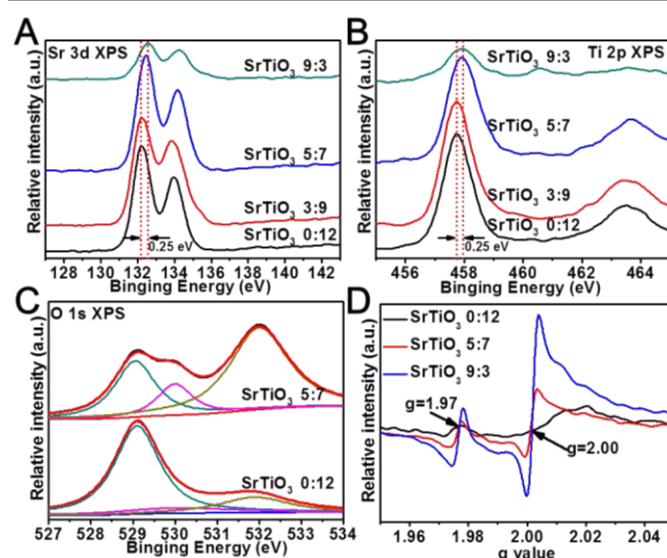
Fig. 2 X-ray photoelectron spectroscopy (XPS) of Sr 3d (A) and Ti 2p (B) of SrTiO$_3$ (0:12, 3:9, 5:7 and 9:3). The O 1s XPS spectra (C) of SrTiO$_3$ (0:12 and 5:7) can be described as the superposition of three peaks by Gaussian distribution, located around 529.2 eV, 530.0 eV and 531.9 eV, respectively. D is the electron paramagnet resonance (EPR) spectra of SrTiO$_3$ (0:12, 5:7 and 9:3).

Surface photovoltage spectroscopy (SPS) is a powerful tool to characterize charge separation at the nanoscale.[37] It was recorded on powder samples sandwiched between an ITO electrode and Cu substrate. Fig. 3A exhibits surface photovoltage (SPV) response of SrTiO$_3$ nanocubes (0:12, 3:9, 5:7 and 9:3). A strong SPV response band in the range 3.3–4.0 eV is observed, which is assigned to the electron transition from valence band to conduction band of SrTiO$_3$ (band–band transition). According to the principle of the SPS, n type semiconductor gives a positive response due to energy band bending up at the interface between n-type semiconductor and metal. And photogenerated electron tends to flow inside of

semiconductor.[37] When the oxygen vacancies (Ti^{3+}) was introduced into $SrTiO_3$, the SPV response turns into negative, indicating that photogenerated electron tends to flow outside (defect site). The defective $SrTiO_3$ changes from original n-type character into p-type nature. We can treat the defective $SrTiO_3$ as Ti^{3+} doped $SrTiO_3$, and Ti^{3+} acts as an electron acceptor, which promotes the photogenerated electron rapidly inject into defect site. This process prevents the electron and hole from recombination. However, $SrTiO_3$ 6:6, 7:5 and 9:3 samples exhibit no SPV response at all. There are following possible reasons for that. One is that the amount of photoinduced electrons accumulating instantly at oxygen vacancy band is so much due to excess oxygen vacancies that photoelectrons can indirectly recombination with holes. Another is that an excess amount of oxygen vacancies can produce the recombination centers of photoinduced electron and hole pairs.[38] In addition, doping a semiconductor with heteroatom (impurities or dopant) can alter the electrical conductivity by many orders of magnitude.[39] For example, Nozik found that the conductivity of Cd_2SnO_4 with oxygen vacancies can raise up about 5 orders of magnitude.[40] SPS is a technique measured the open voltage, which build up by light irradiation. The photocharges are hardly accumulated due to high conductivity of semiconductor. So, SPV response is relatively weak for the high conductivity samples. These factors are responsible for the decrease in the SPS intensity. Very recently, Osterloh demonstrated that the SPS intensity tends to decrease when the photocatalyst directly contact with electron acceptor like metal nanoparticle or redox reagents.[41] In our case, the defects (oxygen vacancies or Ti^{3+}) could work as an electron acceptor. That is reason for a decreased SPS signal or even no signal was observed when the defects were incorporated into the $SrTiO_3$ nanocrystals.
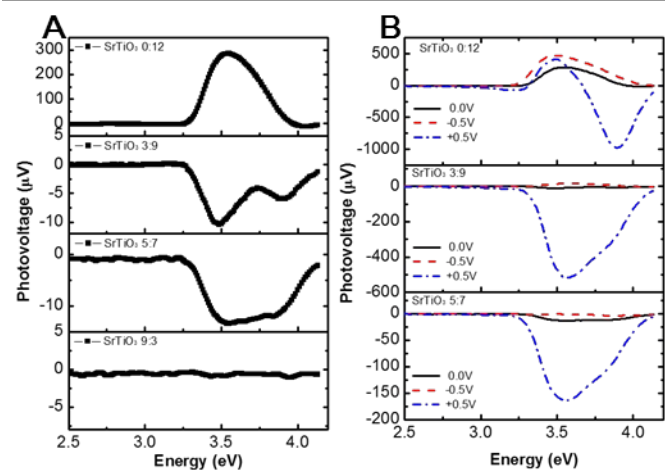
Fig. 3 Surface photovoltage spectroscopy (SPS) of $SrTiO_3$ (0:12, 3:9, 5:7 and 9:3) (A); Field-induced SPS of $SrTiO_3$ (0:12, 3:9 and 5:7) (B).

Field-induced SPS (FISPS) is a technique that combines the electric field effect principle with the SPS, it was employed to further confirm the change of conduction type of $SrTiO_3$ samples.[42] In general, the effects of an external electric field on a semiconductor mainly involve two conditions. One is the electric field may promote the separation efficiency of the photoinduced charge carriers. The other is the electric field may

alter the barrier shape of trapping, leading to the captured charge carriers in the trap easily released. For an n type semiconductor, when a negative bias is applied, the SPV response increases in original direction. If a positive electric field is applied, whose direction is reverse to that of the build-in field, the intensity of SPV response is weakened and even in the reverse direction.[43] In contrast to the n-type semiconductor, the SPS response intensity of p-type semiconductor increases as a positive field is applied and reduces as a negative electric field is applied. Fig. 3B shows the dependence of SPS response of $SrTiO_3$ with different amount of oxygen vacancies. The black line is the SPV response of sample at 0 V bias. The red dash and blue dots lines are the SPS response measured at -0.5 and +0.5 V bias, respectively. In the case of $SrTiO_3$ 0:12, the original response is positive, its intensity of SPS increases when a negative bias field is applied. The SPV signal gradually reduces and turns into reverse response (Fig. S8). These different responses imply that $SrTiO_3$ 0:12 takes on n-type character. For the $SrTiO_3$ 3:9 and 5:7 samples, they exhibit negative response. Their SPV response increase when the negative bias field is applied, and reduce in the case of negative bias field is exerted. These results further confirm that $SrTiO_3$ 0:12 takes on n-type nature and $SrTiO_3$ 3:9 and 5:7 show p-type character.
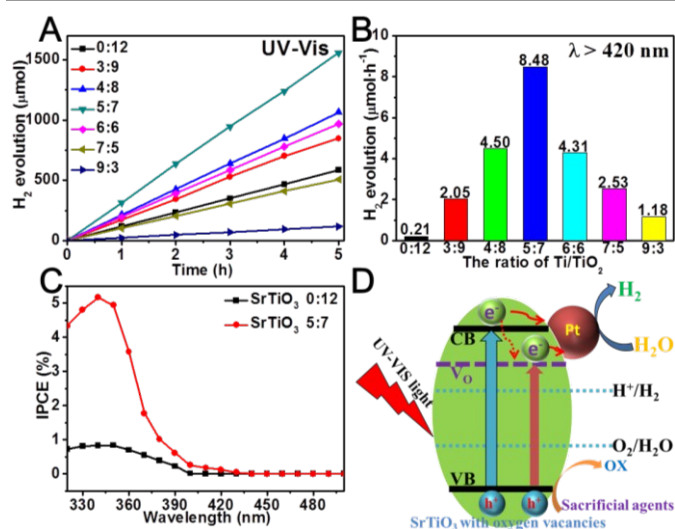
Fig. 4 A) H_2 production of $SrTiO_3$ (0:12, 3:9, 4:8, 5:7, 6:6, 7:5 and 9:3) under UV-Vis light irradiation. B) H_2 production rate of $SrTiO_3$ (0-9:12-3) under visible light ($\lambda > 420$ nm) irradiation. C) IPCE of $SrTiO_3$ 0:12 and 5:7 collected at an applied potential of 0.3 V versus Ag/AgCl. The possible H_2 production mechanism (D) of defective $SrTiO_3$ under UV-Vis light irradiation.

Photoluminescence (PL) spectroscopy is a power tool for characterization of the charge separation. As shown in Fig. S9, $SrTiO_3$ exhibits emission bands at 425 and 470 nm under excitation of 380 nm light. These two emission bands reduce with the increase of defects, indicating that the defects effectively suppress the radiation recombination. In other words, defects promote the charge separation. The Brunauer–Emmett–Teller (BET) surface area and pore size are characterized using N_2 adsorption–desorption isotherm shown in Fig. S10. It presents a type-III isotherm with a type-D hysteresis loop, indicating a macroporous structure.[44-46] The BET surface area are determined to be 9.04, 11.89 and 12.41 m^2/g of $SrTiO_3$ (0:12, 5:7 and 9:3), which illustrates a slight

Nanoscale Accepted Manuscript

variation of BET surface area with the increasing of molar ratio (Ti/TiO_2).

Fig. 4A and S11A show the H_2 production of $SrTiO_3$ when loaded with 1 wt% Pt as cocatalyst under UV-Vis light (300 W Xe lamp). The H_2 production rate is 117.3 μmol/h for 50 mg of $SrTiO_3$ (0:12). With the increasing of molar ratio (Ti/TiO_2), the H_2 production rate increases. However, excess amount of Ti/TiO_2 (6:6, 7:5 and 9:3) results in the high oxygen vacancy concentration and a decrease of H_2 production rate. The optimal molar ratio (Ti/TiO_2) is about 5:7, the corresponding H_2 production rate is 311.8 μmol/h (UV-Vis), which exhibits 2.7 times than $SrTiO_3$ (0:12). Although the bandgap of $SrTiO_3$ (5:7) is ~ 3.16 eV (~ 390 nm), the defective $SrTiO_3$ samples still exhibit a certain visible light H_2 production capability. Fig. 4B and S11B shows the H_2 production of $SrTiO_3$ under visible light irradiation (λ > 420 nm). The H_2 production rate of optimal $SrTiO_3$ 5:7 is 8.5 μmol/h for 50 mg of photocatalyst. To understand that, the incident photon conversion efficiency (IPCE) is measured for $SrTiO_3$ 0:12 and 5:7 samples. Fig. 4C clearly shows the conversion efficiency is about 5 times promotion at 350 nm due to the introduction of defects, indicating that defects can promote the charge separation process. The light response is up to 400 nm for $SrTiO_3$ 0:12. However, the light response can reach 430 nm for $SrTiO_3$ 5:7 sample. These results illustrate that the defects energy band is composed of multiple energy levels. The transition between VB and defects energy band can also be used for H_2 production. That means the defects energy band extend the light response range. The defective $SrTiO_3$ have an excellent stability according to the recycles measure of photocatalytic H_2 production (Fig. S11C and D). After six recycles, none of recession of photocatalytic activity is observed. These results absolutely indicate the oxygen vacancies can narrow the bandgap of $SrTiO_3$ and promote the charge separation of photo generated charge carriers (Fig. 4D).[47-49]

Conclusions

Defective $SrTiO_3$ nanocubes were synthesized via one-step molten salts route by using $SrCO_3$ as Sr source, TiO_2 and Ti powders as Ti source. The Ti^{3+} or oxygen vacancies were successfully kept at high temperature and air environment. SPS results indicated that the conduction type turns from pristine n-type into p-type with the introduction of defects. These defects extend the $SrTiO_3$ light absorption range from UV into visible light region and promote the charge separation efficiency.

Acknowledgements

Notes and references

1. A. Bhalla, R. Guo and R. Roy, *Mater. Res. Innovations*, 2000, **4**, 3-26.
2. M. Pena and J. Fierro, *Chem. Rev.*, 2001, **101**, 1981-2018.
3. C. D. Chandler, C. Roger and M. J. Hampden-Smith, *Chem. Rev.*, 1993, **93**, 1205-1241.
4. M. Zeng, H. Wang, C. Zhao, J. Wei, W. Wang and X. Bai, *Sci. Bull.*, 2015, **60**, 1426-1433.
5. B. Jalan, R. Engel-Herbert, T. E. Mates and S. Stemmer, *Appl. Phys. Lett.*, 2008, **93**.
6. H. Kato and A. Kudo, *J. Phys. Chem. B*, 2002, **106**, 5029-5034.
7. M. Janousch, G. I. Meijer, U. Staub, B. Delley, S. F. Karg and B. P. Andreasson, *Adv. Mater.*, 2007, **19**, 2232-2235.
8. H. Irie, Y. Maruyama and K. Hashimoto, *J. Phys. Chem. C*, 2007, **111**, 1847-1852.
9. H. Tan, Z. Zhao, W.-b. Zhu, E. N. Coker, B. Li, M. Zheng, W. Yu, H. Fan and Z. Sun, *ACS Appl. Mater. Interfaces*, 2014, **6**, 19184-19190.
10. W. L. Harrigan, S. E. Michaud, K. A. Lehuta and K. R. Kittilstved, *Chem. Mater.*, 2016, **28**, 430-433.
11. F. Wagner and G. Somorjai, *Nature*, 1980, **285**, 559-560.
12. S. Ouyang, H. Tong, N. Umezawa, J. Cao, P. Li, Y. Bi, Y. Zhang and J. Ye, *J. Am. Chem. Soc.*, 2012, **134**, 1974-1977.
13. L. Chen, S. Zhang, L. Wang, D. Xue and S. Yin, *J. Cryst. Growth*, 2009, **311**, 746-748.
14. S. Ohta, T. Nomura, H. Ohta, M. Hirano, H. Hosono and K. Koumoto, *Appl. Phys. Lett.*, 2005, **87**, 092108.
15. H. Ohta, S. Kim, Y. Mune, T. Mizoguchi, K. Nomura, S. Ohta, T. Nomura, Y. Nakanishi, Y. Ikuhara and M. Hirano, *Nat. Mater.*, 2007, **6**, 129-134.
16. X. Fan, Y. Wang, X. Chen, L. Gao, W. Luo, Y. Yuan, Z. Li, T. Yu, J. Zhu and Z. Zou, *Chem. Mater.*, 2010, **22**, 1276-1278.
17. J. Huang, R. Ma, Y. Ebina, K. Fukuda, K. Takada and T. Sasaki, *Chem. Mater.*, 2010, **22**, 2582-2587.
18. S. C. Yan, S. X. Ouyang, J. Gao, M. Yang, J. Y. Feng, X. X. Fan, L. J. Wan, Z. S. Li, J. H. Ye and Y. Zhou, *Angew. Chem. Int. Ed.*, 2010, **49**, 6400-6404.
19. J. Yang, D. Wang, H. Han and C. Li, *Acc. Chem. Res.*, 2013, **46**, 1900-1909.
20. L. Mei, H. Zhao and B. Lu, *Adv. Sci.*, 2015, **2**, 201500116.
21. Z. Zhao, X. Zhang, G. Zhang, Z. Liu, D. Qu, X. Miao, P. Feng and Z. Sun, *Nano Res.*, 2015, **8**, 4061-4071.
22. C. Zhou, Y. Zhao, L. Shang, Y. Cao, L.-Z. Wu, C.-H. Tung and T. Zhang, *Chem. Commun.*, 2014, **50**, 9554-9556.
23. Y. Zhao, G. Chen, T. Bian, C. Zhou, G. I. N. Waterhouse, L.-Z. Wu, C.-H. Tung, L. J. Smith, D. O'Hare and T. Zhang, *Adv. Mater.*, 2015, **27**, 7823-7823.
24. W. Yu, G. Ou, W. Si, L. Qi and H. Wu, *Chem. Commun.*, 2015, **51**, 15685-15688.
25. F. Dang, K.-i. Mimura, K. Kato, H. Imai, S. Wada, H. Haneda and M. Kuwabara, *CrystEngComm*, 2011, **13**, 3878-3883.
26. Z. Zhao, H. Tan, H. Zhao, Y. Lv, L.-J. Zhou, Y. Song and Z. Sun, *Chem. Commun.*, 2014, **50**, 2755-2757.
27. C. Lee, J. Destry and J. L. Brebner, *Phys. Rev. B*, 1975, **11**, 2299-2310.
28. W. S. Baer, *Phys. Rev.*, 1966, **144**, 734-738.
29. T. Sun and M. Lu, *Appl. Phys. A*, 2012, **108**, 171-175.
30. T. Kawabe, K. Tabata, E. Suzuki, Y. Yamaguchi and Y. Nagasawa, *J. Phys. Chem. B*, 2001, **105**, 4239-4244.
31. S.-M. Park, T. Ikegami and K. Ebihara, *Thin Solid Films*, 2006, **513**, 90-94.
32. M. Chen, X. Wang, Y. Yu, Z. Pei, X. Bai, C. Sun, R. Huang and L. Wen, *Appl. Surf. Sci.*, 2000, **158**, 134-140.
33. F. Zuo, K. Bozhilov, R. J. Dillon, L. Wang, P. Smith, X. Zhao, C. Bardeen and P. Feng, *Angew. Chem.*, 2012, **124**, 6327-6330.
34. M. K. Kumar, K. Bhavani, B. Srinivas, S. N. Kumar, M. Sudhakar, G. Naresh and A. Venugopal, *Appl. Catal. A*, 2016, **515**, 91-100.
35. S. Livraghi, A. Votta, M. C. Paganini and E. Giamello, *Chem. Commun.*, 2005, 498-500.
36. G. Barolo, S. Livraghi, M. Chiesa, M. C. Paganini and E. Giamello, *J. Phys. Chem. C*, 2012, **116**, 20887-20894.
37. L. Kronik and Y. Shapira, *Surf. Sci. Rep.*, 1999, **37**, 1-206.
38. J. Liqiang, F. Honggang, W. Baiqi, W. Dejun, X. Baifu, L. Shudan and S. Jiazhong, *Appl. Catal. B Environ.*, 2006, **62**, 282-291.
39. H. J. Queisser and E. E. Haller, *Science*, 1998, **281**, 945-950.
40. A. J. Nozik, *Phys. Rev. B*, 1972, **6**, 453.
41. J. Wang, J. Zhao and F. E. Osterloh, *Energy Environ. Sci.*, 2015, **8**, 2970-2976.
42. J. Liqiang, Q. Yichun, W. Baiqi, L. Shudan, J. Baojiang, Y. Libin, F. Wei, F. Honggang and S. Jiazhong, *Solar Energy Mater. Solar Cells*, 2006, **90**, 1773-1787.
43. X. Tengfeng, W. Dejun, Z. Lianjie, W. Ce, L. Tiejin, Z. Xueqin and W. Mang, *J. Phys. Chem. B*, 2000, **104**, 8177-8181.
44. D. Liu, Y. Yao, D. Tang, S. Tang, Y. Che and W. Huang, *Int. J. Coal Geol.*, 2009, **79**, 97-112.
45. M. Khalfaoui, S. Knani, M. Hachicha and A. B. Lamine, *J. Colloid Interface Sci.*, 2003, **263**, 350-356.
46. J. Wang, X. Yang, D. Wu, R. Fu, M. S. Dresselhaus and G. Dresselhaus, *J. Power Sources*, 2008, **185**, 589-594.
47. Z. Zhang, W. Wang, E. Gao, M. Shang and J. Xu, *J. Hazard. Mater.*, 2011, **196**, 255-262.
48. T.-T. Chen, I.-C. Chang, M.-H. Yang, H.-T. Chiu and C.-Y. Lee, *Appl. Catal. B: Environ.*, 2013, **142**, 442-449.
49. L. Liu, F. Gao, H. Zhao and Y. Li, *Appl. Catal. B: Environ.*, 2013, **134**, 349-358.

Nanoscale Accepted Manuscript